NANO LETTERS

pubs.acs.org/NanoLett Letter

Charge Carrier Dynamics at the Interface of 2D Metal−Organic Frameworks and Hybrid Perovskites for Solar Energy Harvesting

Robert Stanton and Dhara J. Trivedi*

Cite This: https://doi.org/10.1021/acs.nanolett.3c04054 Read Online

ACCESS | Metrics & More | Article Recommendations | Supporting Information

ABSTRACT: Interfacing perovskites with two-dimensional materials such as metal−organic frameworks (MOFs) for improved stability and electron or hole extraction has emerged as a promising path forward for the generation of highly efficient and stable solar cells. In this work, we examine the structural properties and excitation dynamics of two MOF−perovskite systems: UMCM309-a@$MAPbI_3$ and ZrL3@$MAPbI_3$. We find that precise band alignment and electronegativity of the MOF-linkers are necessary to facilitate the capture of excited charge carriers. Furthermore, we demonstrate that intraband relaxation of hot electrons to the MOF subsystem results in optically disallowed transitions across the band gap, suppressing radiative recombination. Furthermore, we elucidate the key mechanisms associated with improved structural stability afforded to the perovskites by the two-dimensional MOFs, highlighting the necessity of broad surface coverage and strong MOF−perovskite interaction.

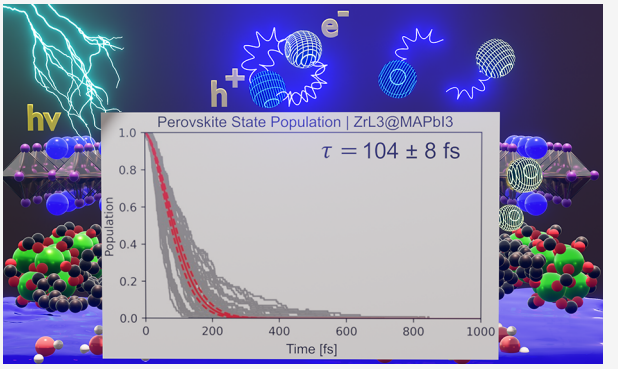

KEYWORDS: *photovoltaics, metal−organic framework, perovskite, two-dimensional materials, electron extraction layer, nonadiabatic molecular dynamics*

Perovskites have become ubiquitous for usage in solar energy harvesting applications, and research efforts have characterized large subsets of this class of materials ranging from perovskite oxides to hybrid organic−inorganic perovskites.[1−3] Even more recently, perovskites of reduced dimensionality and mixed cations have become promising avenues of investigation.[4−9] Given the long history of research into perovskite-based solar energy harvesting, they have been demonstrated to exhibit some of the highest power conversion efficiencies among single junction solar cells, reaching as high as 25.7%.[10] However, the most successful lead-based perovskite materials are plagued by issues of stability and device longevity.[11−15] These issues of structural integrity are only exacerbated by the leakage of toxic building components into the environment upon degradation, which poses problems for their implementation in environmentally conscious and sustainable clean energy applications. This has led to both the search for lead-free alternatives within the class of perovskite materials and efforts to mitigate these structural concerns through the proximal interfacing of perovskites with stabilizing two-dimensional (2D) materials such as monolayer graphene, graphitic carbon nitride, and metal−organic frameworks (MOFs).[16−24] The latter is the focus of the current investigation, whereby we explore passivation of the surface of an $MAPbI_3$ thin film with the ZrL3 MOF (and its unfunctionalized analogue, UMCM-309a) which has undergone experimental synthesis by Wu et al. and showed promise as a stable and efficient mixed-material perovskite-based solar cell.[25]

MOFs are a class of nanoporous materials that consist of metal oxide clusters connected through a network of organic ligands, generating a family of crystalline frameworks which are incredibly diverse in their structural and electronic properties. Of particular interest to the synthesis of MOF−perovskite systems is the ability to tune key material characteristics such as the presence of chemically active groups at the MOF−perovskite interface and the amount of surface coverage offered by the MOF.[26−28] The interplay of these factors allows for precise control over the resulting hybrid device properties by increasing the ease of charge extraction, passivating or exploiting defects, and mitigating or preventing the environmental effects associated with ion diffusion in the perovskite subsystems.[29,30] The well-established low exciton binding energies present in $MAPbI_3$ have led to many applications involving the utilization of hole extraction layers (HELs) and electron extraction layers (EELs) to facilitate high yield charge

Received: October 23, 2023
Revised: December 12, 2023
Accepted: December 13, 2023

https://doi.org/10.1021/acs.nanolett.3c04054
Nano Lett. XXXX, XXX, XXX−XXX

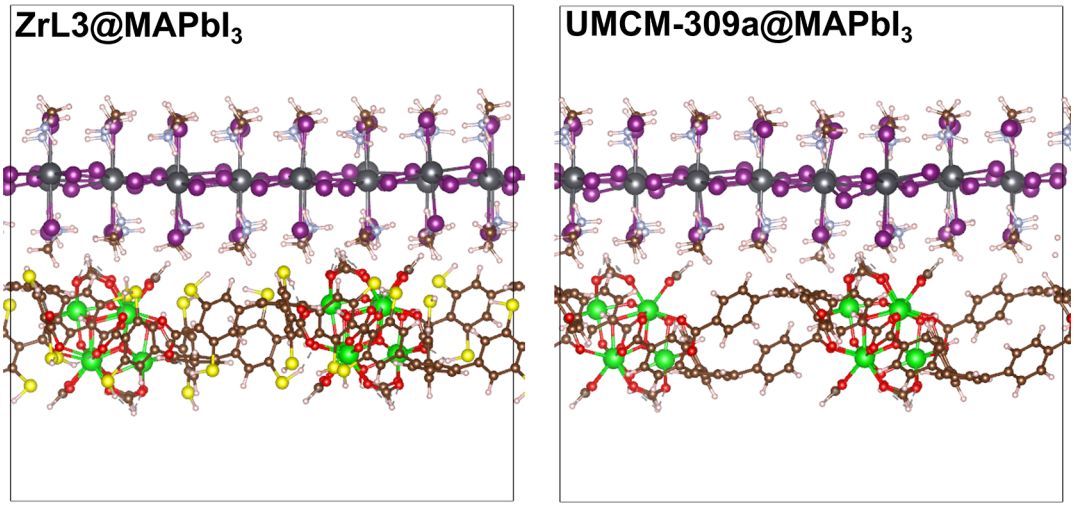

Figure 1. Simulation cells for the ZrL3@$MAPbI_3$ and UMCM-309a@$MAPbI_3$ systems. Geometries pictured have been optimized at the DFT level.

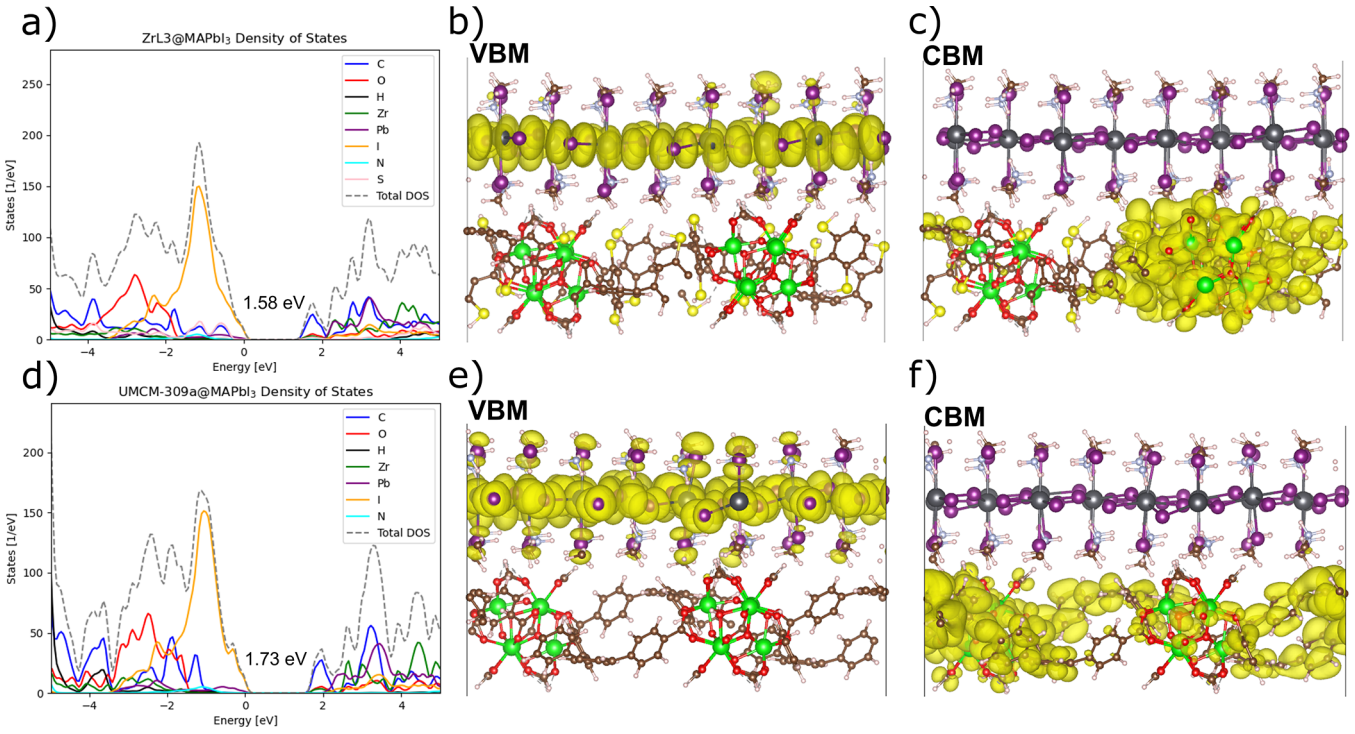

Figure 2. (a, d) Density of states for the ZrL3@$MAPbI_3$ and UMCM-309a@$MAPbI_3$ hybrid MOF−perovskite systems. Band gaps are placed in the inset of the DOS plots representing the minimum energy perovskite to MOF excitation. Lowest energy perovskite to perovskite excitations occur at approximately 2.2 eV in both cases. (b, c) VBM and CBM wave functions for the ZrL3@$MAPbI_3$ system. (e, f) VBM and CBM wave functions for the UMCM-309a@$MAPbI_3$ system.

extraction and thereby drastically improved photovoltaic performance.[31−33] One such example is an investigation by Wu et al., who synthesized the previously mentioned MOF−perovskite system consisting of $MAPbI_3$ and a thiol-functionalized version of the 2D UMCM-309a MOF (ZrL3) as an EEL.[25] This system was determined to serve the dual purpose of increasing device longevity by way of mitigating lead leakage while simultaneously rapidly suppressing photoluminescence relative to that observed in the pure perovskite sample.

In this work, we conduct a comprehensive computational investigation of the structural and excitation dynamics associated with the UMCM-309a and ZrL3MOFs interfaced with the $MAPbI_3$ perovskite system (Figure 1). The UMCM-309a MOF employs the commonly seen $Zr_6(OH)_4(O)_4$ node and a tritopic 1,3,5-(4-carboxylphenyl)benzene linker.[34] We utilize a multiscale computational framework including density functional theory (DFT) and extended tight binding (xTB) calculations to gain insight regarding the geometric and electronic structure relevant to these hybrid systems.[35,36] We carry out nonadiabatic molecular dynamics (NA-MD) simulations on both the pristine and thiol-functionalized version of the MOF−perovskite system to highlight the importance of electronegative functional groups in the MOF ligands for facilitating rapid charge extraction. Finally, we carry out extensive molecular dynamics (MD) simulations involving the explicitly solvated MOF−perovskite system to elucidate

https://doi.org/10.1021/acs.nanolett.3c04054
Nano Lett. XXXX, XXX, XXX−XXX

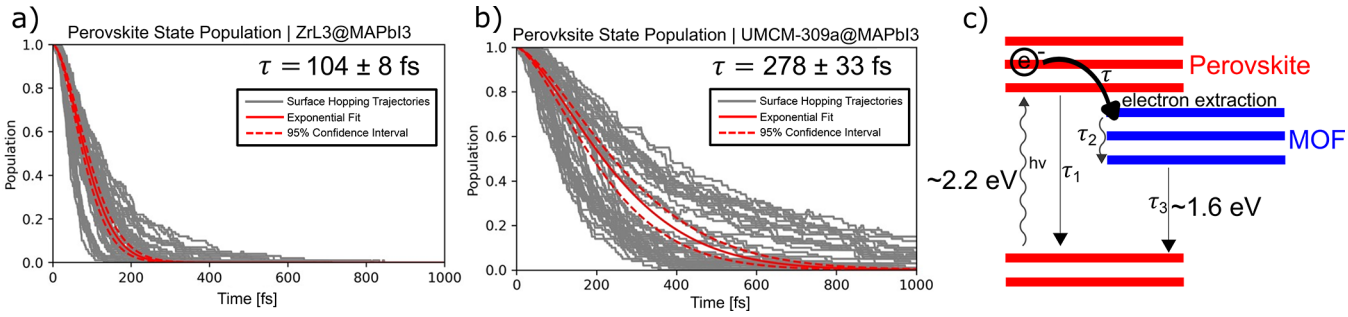

Figure 3. (a, b) Perovskite to MOF electron extraction in the ZrL3@MAPbI$_3$ and UMCM-309a@MAPbI$_3$ systems, respectively. Thiol functionalization of the ligands in the ZrL3MOF can be seen to drastically increase the speed of charge extraction. (c) Schematic representation of the competing time scales present in the hybrid MOF−perovskite systems.

the previously discovered mitigation of lead leakage by Wu et al.

The interfaced MOF−perovskite system was constructed by orthogonalizing the unit cell of the UMCM-309a MOF, resulting in a structure with two Zr_6 clusters per cell, twice that of the primitive unit cell with *P*-3 symmetry. A 2 × 3 × 1 supercell of the MAPbI$_3$ perovskite system represented the nearest match to the corresponding lattice parameters of the orthogonalized UMCM-309a system. The resulting difference between cells was split equally, and the interfaced system corresponds to 2% and 4% tensile strain along the *x*- and *y*-directions per MAPbI$_3$ unit cell and 2% and 5% compressive strain along the resultant *x*- and *y*-directions per UMCM-309a unit cell. The interfaced system was found to interact primarily by way of weak dispersive interactions, resulting in Pb−Zr distances of 7−8 Å (Figures S2 and S3). To investigate the effect of electronegative functional groups present in the MOF ligand on electron extraction, we employ all subsequent calculations on both the bare UMCM-309a@MAPbI$_3$ system and the thiol-functionalized analogue to the ZrL3 system investigated by Wu et al., herein termed ZrL3@MAPbI$_3$. The simulation cells of both structures containing over 600 atoms were then optimized at the DFT level using GPAW, and single point calculations were performed to obtain eigenstates at the band extrema (Figure 2b,c,e,f), density of states (Figure 2a,d), electronic band gaps, and optimized structural properties.[37] MD and NA-MD calculations are all performed at the xTB level using the CP2K package together with the xTB-NA-MD framework developed by Shakiba et al. as implemented in the Libra software package.[38−41] Additional computational details regarding all calculations can be found in the Supporting Information.

Structural implications of the strain applied to the materials that is necessary to facilitate commensurate lattice parameters had little impact on the MOF and perovskite subsystems.[42] The resulting structures had an average Pb−I bond distance of 3.23 and 3.24 Å for the UMCM-309a and ZrL3 interfaced MAPbI$_3$ systems, respectively. Additionally, for both systems, *cis* and *trans* Pb−I−Pb bond angles center around 90° and 175°, respectively (Figure S1), which are in line with previous investigations of MAPbI$_3$ and its 2D analogues.[43−45] The density of states (DOS) of UMCM-309a@MAPbI$_3$ and its thiol-functionalized analogue ZrL3@MAPbI$_3$ are pictured in Figures 2a and 2d, respectively. Contributions from the perovskite subsystem remained consistent for both structures with a gap between frontier perovskite-localized eigenstates of approximately 2.2 eV, marking the transition between occupied states with I(p) and Pb(s) character and unoccupied states with Pb(p) character. Interfacing MAPbI$_3$ with the 2D-MOFs modified the electronic structure via introduction of numerous midgap states associated with both the Zr-oxide nodes and the organic ligands. The close energetic proximity of the introduced states to the conduction band (CB) of the perovskite subsystem aids in explaining the previously established efficiency of the ZrL3 MOF as an electron extraction layer (EEL) by Wu et al.[25] The conduction band minima (CBM) of the UMCM-309a@MAPbI$_3$ system is largely localized to the organic ligand of the MOF, while the thiol-functionalized CBM has an increased contribution of the Zr oxide node (Figure 2). In both systems, the valence band maximum (VBM) consists of the I(5p) orbitals as in the case of the bulk MAPbI$_3$ system.[46] The lowest energy transition of the materials varied in accordance with the electronegativity of the organic ligand. The thiol-functionalized ZrL3@MAPbI$_3$ system exhibited a band gap of 1.58 eV compared to that of the unfunctionalized UMCM-309a@MAPbI$_3$ which yielded a band gap of 1.73 eV. We find these differences in electronic structure to have large implications for the efficiency of these hybrid MOF−perovskite systems when considering their respective excitation dynamics.

To investigate the excitation dynamics in the hybrid MOF−perovskite systems, we performed NA-MD simulations with a 3 ps duration and 0.5 fs time step to accurately capture the rapid dynamics associated with movements of the organic components in the MOF and perovskite subsystems. For assessment of the time scales associated with electron extraction, and thereby the efficiency of the two MOFs as EELs, we note the stark energetic separation of the MOF-localized states near the CB edge from those with mixed or perovskite character (Figure 2a,d and Figures S4−S5). To quantify the localization of eigenstates to the MOF subsystem, we computed $\rho_{MOF} = \int_{\Omega_{MOF}} \psi_n^* \psi_n \, d^3r$, where n denotes state index in the xTB calculation and Ω_{MOF} denotes the volume of the simulation cell occupied by the UMCM-309a and ZrL3 MOFs. ρ_{MOF} was computed for the first 100 CB states at selected intervals along the MD trajectory (Figures S4 and S5), and we use a minimum of 70% charge localization to determine the state index below which all CB states strongly confine electronic charge to the MOF. With this heuristic established, characterization of electron extraction is straightforward and can be performed by considering summed populations of states in the MOF and perovskite subsystems.

We consider excitations into optically active states localized to the CB of the perovskite substructure and observe time scales of the subsequent intraband relaxation of electrons to

https://doi.org/10.1021/acs.nanolett.3c04054
Nano Lett. XXXX, XXX, XXX−XXX

the band edge (Figure 3c). In the context of UMCM-309a@$MAPbI_3$ and ZrL3@$MAPbI_3$, relaxation to the band edge is equivalent with perovskite-to-MOF charge extraction due to the energetic ordering of eigenstates (Figures S4 and S5). As previously mentioned, the electronegativity of the ligand was found to have a dramatic impact on the rapidity of electron extraction, indicating between a 2.39- and 2.67-fold speedup in the time scale of charge extraction (Table 1). We briefly note

Table 1. NA-MD Time Scales for the ZrL3@$MAPbI_3$ and UMCM-309A@$MAPbI_3$ Systems Using the FSSH, MSDM, and IDA Methods

method	ZrL3@$MAPbI_3$ time scale (fs)	UMCM-309a@$MAPbI_3$ time scale (fs)	relative speedup
FSSH	104 ± 8	278 ± 9	2.67
mSDM	107 ± 9	277 ± 31	2.59
IDA	438 ± 31	1048 ± 135	2.39

that while electronegativity aids in the extraction of charges at a rapid rate, it is also necessary that the newly introduced MOF states align favorably in the DOS, that is, just below the CBM (VBM) for EELs (HELs). These results suggest that the search for favorable band alignment in similar MOFs containing increasingly electronegative ligands may be a particularly fruitful avenue of future research for mixed-material perovskite-based solar energy harvesting devices.

Additionally, in both the ZrL3@$MAPbI_3$ system and the UMCM-309a@$MAPbI_3$ system, NA-MD simulations demonstrated that the mixed character of states higher in the CB may aid in accelerating the intraband relaxation, even relative to that of the bare perovskite. A representative example of these mixed states in the conduction band can be found in Figure S8 whereby contributions from the MOF subsystem come in the form primarily of C(p), O(p), and Zr(d) orbitals, while the perovskite contribution is largely from Pb(p) and I(p) orbitals. Typical intraband relaxation in $MAPbI_3$ and similar analogues exhibits time scales between 100 and 1000 fs relatively consistently across the literature.[47−49] Time scales associated with the electron extraction for all surface hopping methods in the present study can be found in Table 1. Fewest switches surface hopping (FSSH) and modified simple decay of mixing (mSDM) treatments of the excited state dynamics yielded similar time scales, τ, for the intraband relaxation and thereby perovskite−MOF charge extraction.[50,51] For the ZrL3-containing system we found τ = 104 and 107 fs respectively for FSSH and mSDM. In the unfunctionalized UMCM-309a-containing system, however, we find time scales of τ = 278 and 277 fs, again for FSSH and mSDM, respectively. Treatment of excitation dynamics with instantaneous decoherence at attempted surface hops (IDA) significantly slowed the relaxation to τ = 438 and 1048 fs for the ZrL3 and UMCM-309a containing systems, respectively.[52] It is well established that this instantaneous treatment of decoherence serves to slow the time scales associated with population transfer to low-lying states. Furthermore, this is exacerbated by the fact that the low-lying states in the ZrL3@$MAPbI_3$ and UMCM-309a@$MAPbI_3$ systems all exhibit strongly localized character to the MOF subsystem.[52−54]

We did not treat radiative recombination of charge carriers using NA-MD in the present study; however, we note that the rapid time scales of electron extraction are highly favorable for usage in EELs. The time scales of intraband relaxation of the perovskite subsystem and subsequent radiative recombination associated with optically active Pb(p)−I(p) transitions (τ_1 in Figure 3) must compete with those associated with perovskite−MOF charge extraction, intraband relaxation to the band edge of the MOF (τ in Figure 3), and the subsequent radiative or nonradiative recombination (τ_2 in Figure 3). To assess the viability of MOF−perovskite radiative recombination, we compute the transition dipole moments (TDMs) at the DFT level between the VBM and the first 100 CB states in Figures S6 and S7. We note that upon relaxation to the CB of the MOF, radiative recombination becomes almost entirely disallowed due to the near zero TDM between states. This together with the rapid time scales of perovskite−MOF charge extraction aids in explaining the suppression of photoluminescence observed by Wu et al. in the experimentally synthesized ZrL3@$MAPbI_3$ system. Given the efficient electron extraction coupled with optically disallowed transitions from the band edge of the MOF to the perovskite system, nonradiative recombination is required to facilitate the majority of lost charge carriers. However, due to the spatial and energetic separation between frontier orbitals of the MOF and perovskite subsystems, nonradiative losses will be increasingly frustrated, improving the efficiency of the mixed-material devices. The combination of suppressed radiative recombination through optically disallowed transitions upon rapid charge extraction together with difficult to facilitate nonradiative recombination owing to large spatial and energetic separation aids in explaining the promise of the ZrL3 and UMCM-309a MOFs as efficient EELs in the mixed-material perovskite-based solar energy harvesting devices. Additionally, the electronegativity of the ligand in the ZrL3 MOF serves to accelerate intraband relaxation nearly 3-fold, thereby aiding in suppressing the potential for loss of excited charge carriers through perovskite−perovskite recombination. The functionalization of the capping MOF layers has the potential to aid not only in the facilitation of rapid charge extraction but also in the increased stability of the perovskite subsystem.

To analyze the stability conferred to the perovskite system through interfacing with the UMCM-309a and ZrL3 MOFs, we performed xTB MD simulations of the interfaced MOF−perovskite systems. The void regions of the simulation cells were initialized with water molecules using PackMol at the standard density of water (278 water molecules in the ZrL3@$MAPbI_3$ system and 300 in the UMCM-309a@$MAPbI_3$ system, Figure S10) both above and below the perovskite and MOF subsystems, respectively. The systems were then equilibrated for 1 ps followed by a 20 ps production run.[55] In the case of both systems, the MOF layer completely and successfully inhibits the translation of water molecules into the perovskite subsystem, whereas even during the 20 ps simulation, the uncapped side of the $MAPbI_3$ thin film begins to allow H_2O penetration into the PbI_6 octahedra. Though we find no moisture penetration through either MOF over the time scales of 20 ps, we note a large difference in the porosity of the optimized UMCM-309a MOF structure compared with that of ZrL3. As seen in Figure S9, UMCM-309a as a capping layer contains large channels through which H_2O molecules can diffuse, allowing for increased access to the perovskite subsystem. In contrast, penetrable channels through which water can permeate ZrL3 are either removed entirely or significantly restricted, in turn reducing the access of guest water molecules to the perovskite. This suggests that not only does ZrL3 efficiently mitigate Pb leakage via the capture of

https://doi.org/10.1021/acs.nanolett.3c04054
Nano Lett. XXXX, XXX, XXX−XXX

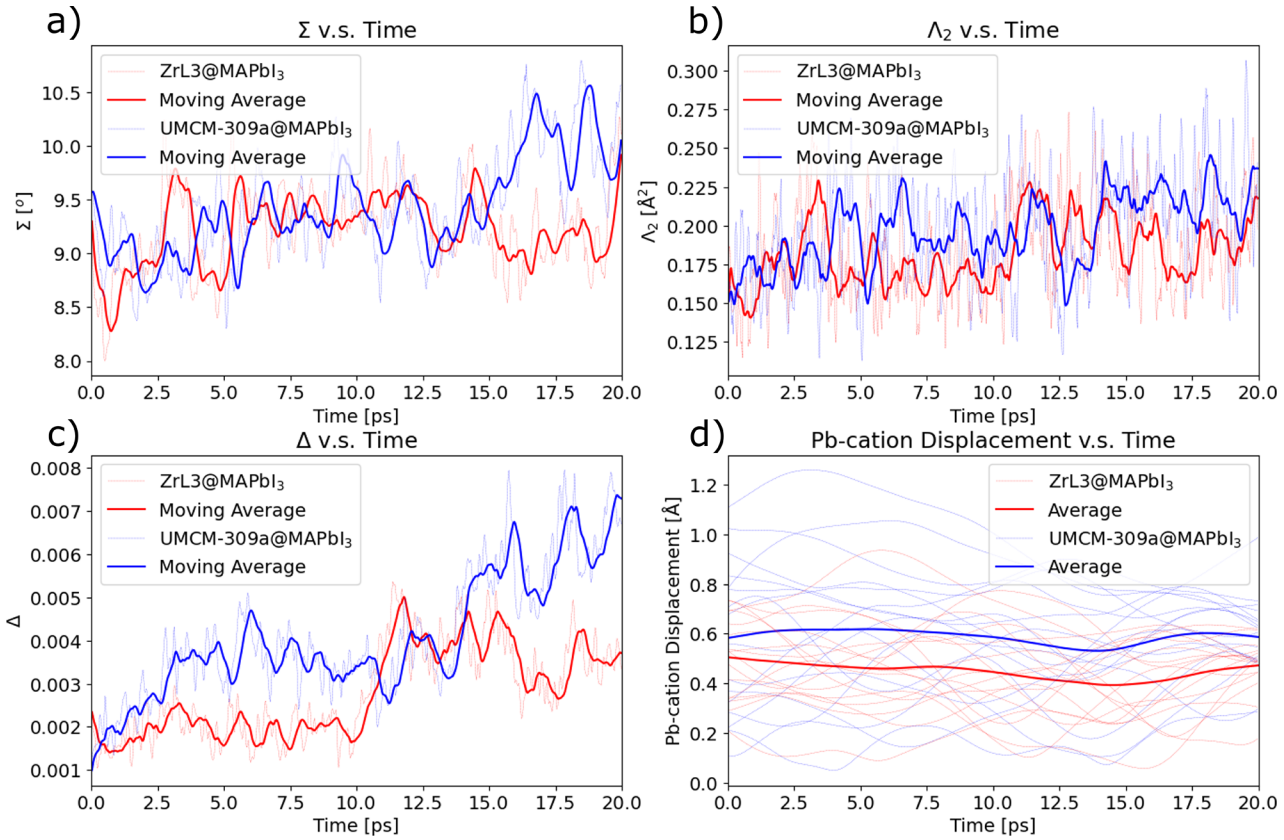

Figure 4. Octahedral distortion parameters over time: (a) Σ representing distortions of I−Pb−I bond angles, (b) Λ_2 representing diagonal dislocations of the Pb cation within the octahedra, (c) Δ representing deviations of the Pb−I bond lengths from the average, and (d) Pb cation displacement over the 20 ps MD trajectory with explicit solvation of the ZrL3@$MAPbI_3$ and UMCM-309a@$MAPbI_3$ systems. Moving averages are defined as the averages of the previous 20 MD steps.

displaced Pb cations observed by Wu et al. (which happens at time scales beyond those accessible through semiempirical methods used in the present study) but also that careful selection of MOFs as capping layers can significantly reduce such moisture-induced cation dislocation to begin with.[25]

Upon consideration of the structural dynamics in the moisture exposed MOF−perovskite systems, we found increased structural stability demonstrated by the ZrL3 interfaced system when compared to that of UMCM-309a by way of numerous metrics including the Σ, Λ_2, and Δ octahedral distortion parameters (Figure 4) and the Pb cation displacement from the optimized geometry along the MD run. Σ and Δ represented distortions from idealized octahedra bond angles and distances respectively, and Λ_2 quantifies diagonal displacements of the Pb cation in the PbI_6 octahedra.[56] Typical octahedral distortions can lead to distortion parameters of up to approximately 15°, 0.1, and 0.75 $Å^2$ for Σ, Δ, and Λ_2, respectively.[56] Perovskite octahedra remain largely intact, even when penetrated by H_2O molecules from the exposed side of the thin film in both systems. Additionally, the structural integrity of both the UMCM-309a and ZrL3MOFs remains intact over the course of the 20 ps simulation. The thiol-functionalized ZrL3 MOF interacts more strongly with guest water molecules by way of transient dispersive S−H--O bonds, potentially aiding even further in reduced moisture penetration compared to that of UMCM-309a. The nodes in both MOFs demonstrate occasional dangling formate ligands and subsequent dispersive C−O--H interaction with nearby H_2O without compromising the stability of the node as we observed in our previous investigation regarding defects present within the $Zr_6(OH)_4(O)_4$ node. By all metrics (Figure 4), after the 20 ps MD simulation, the ZrL3@$MAPbI_3$ exhibits increased structural stability upon exposure to water over its unfunctionalized counterpart UMCM-309a@$MAPbI_3$.

In summary, we present a comprehensive investigation of both the excitation dynamics and structural properties of the hybrid UMCM-309a@$MAPbI_3$ and ZrL3@$MAPbI_3$ systems. Our work highlights the necessity of both band alignment and favorable chemical properties of the interfaced framework for its efficient performance as an EEL or HEL. We demonstrate that charge extraction happens on time scales between 2.39 and 2.67 faster to the ZrL3 MOF owing to increased overlap of states near the CB edge and, more importantly, increased electronegativity of the thiol-functionalized ligand compared to that present in UMCM-309a. The subpicosecond charge extraction and subsequent relaxation of electrons to the CB edge were found to result in optically inactive transitions between the CB and VBM. This demonstrates that in addition to rapid charge extraction, the extraction layers can serve to mitigate radiative recombination by introduction of optically inactive states near the band edge. Furthermore, assessment of the structural stability of both MOF−perovskite systems in the presence of explicit solvation indicates the importance of high surface coverage of the host framework. The $MAPbI_3$ system interfaced with the less porous ZrL3 MOF was, by all metrics, exhibiting increased stability over the more porous UMCM-309a system after 20 ps of MD simulation under the

https://doi.org/10.1021/acs.nanolett.3c04054
Nano Lett. XXXX, XXX, XXX−XXX

consideration of an explicit solvent. This work provides valuable insights for the future design of hybrid MOF−perovskites which aim to facilitate rapid charge extraction while simultaneously conferring increased stability to the perovskite subsystem. Our results suggest that future efforts should focus on favorable band alignment between the two subsystems, high surface coverage of the MOF capping layer, and the presence of electronegative functional groups on the MOF ligand if the MOF is aimed to serve as an EEL.

■ ASSOCIATED CONTENT

Supporting Information

The Supporting Information is available free of charge at https://pubs.acs.org/doi/10.1021/acs.nanolett.3c04054.

Additional computational details; bond angle distributions and partial radial distribution functions for the DFT-optimized MOF−perovskite systems; plots detailing eigenstate localization and transition dipole moments between the excited states and valence band edge; accessible surface area to an H_2O probe molecule in the MOF−perovskite systems; MD snapshots from the explicitly solvated systems (PDF)

■ AUTHOR INFORMATION

Corresponding Author

Dhara J. Trivedi − *Department of Physics, Clarkson University, Potsdam, New York 13699, United States;* orcid.org/0000-0002-8151-3929; Email: dtrivedi@clarkson.edu

Author

Robert Stanton − *Department of Physics, Clarkson University, Potsdam, New York 13699, United States;* orcid.org/0000-0002-4989-6958

Complete contact information is available at: https://pubs.acs.org/10.1021/acs.nanolett.3c04054

Notes

The authors declare no competing financial interest.

■ ACKNOWLEDGMENTS

The authors gratefully acknowledge support from the U.S. National Science Foundation (ECCS-2138728). This work used Bridges-2 at Pittsburgh Supercomputing Center through allocation CHE210004 from the Advanced Cyberinfrastructure Coordination Ecosystem: Services & Support (ACCESS) program, which is supported by National Science Foundation Grants #2138259, #2138286, #2138307, #2137603, and #2138296.

■ REFERENCES

(1) Kumar, A.; Kumar, A.; Krishnan, V. Perovskite Oxide Based Materials for Energy and Environment-Oriented Photocatalysis. *ACS Catal.* **2020**, *10* (17), 10253−10315.

(2) Aranda, C. A.; Caliò, L.; Salado, M. Toward Commercialization of Stable Devices: An Overview on Solar Cells. *Crystals* **2021**, *11* (5), 519.

(3) Xu, W. J.; Kopyl, S.; Kholkin, A.; Rocha, J. Hybrid Organic-Inorganic Perovskites: Polar Properties and Applications. *Coord. Chem. Rev.* **2019**, *387*, 398−414.

(4) Kumavat, S. R.; Sonvane, Y.; Singh, D.; Gupta, S. K. Two-Dimensional CH3NH3PbI3 with High Efficiency and Superior Carrier Mobility: A Theoretical Study. *J. Phys. Chem. C* **2019**, *123* (9), 5231−5239.

(5) Gao, Y.; Wei, Z.; Hsu, S. N.; Boudouris, B. W.; Dou, L. Two-Dimensional Halide Perovskites Featuring Semiconducting Organic Building Blocks. *Mater. Chem. Front.* **2020**, *4* (12), 3400−3418.

(6) Blancon, J. C.; Even, J.; Stoumpos, C. C.; Kanatzidis, M. G.; Mohite, A. D. Semiconductor Physics of Organic−Inorganic 2D Halide Perovskites. *Nat. Nanotechnol.* **2020**, *15* (12), 969−985.

(7) Stoumpos, C. C.; Cao, D. H.; Clark, D. J.; Young, J.; Rondinelli, J. M.; Jang, J. I.; Hupp, J. T.; Kanatzidis, M. G. Ruddlesden-Popper Hybrid Lead Iodide Perovskite 2D Homologous Semiconductors. *Chem. Mater.* **2016**, *28* (8), 2852−2867.

(8) Charles, B.; Dillon, J.; Weber, O. J.; Islam, M. S.; Weller, M. T. Understanding the Stability of Mixed A-Cation Lead Iodide Perovskites. *J. Mater. Chem. A* **2017**, *5* (43), 22495−22499.

(9) Yılmaz, B.; Odabaşı, Ç.; Yıldırım, R. Efficiency and Stability Analysis of 2D/3D Perovskite Solar Cells Using Machine Learning. *Energy Technol.* **2022**, *10* (3), 1−12.

(10) Gharibzadeh, S.; Hossain, I. M.; Fassl, P.; Nejand, B. A.; Abzieher, T.; Schultes, M.; Ahlswede, E.; Jackson, P.; Powalla, M.; Schäfer, S.; Rienäcker, M.; Wietler, T.; Peibst, R.; Lemmer, U.; Richards, B. S.; Paetzold, U. W. 2D/3D Heterostructure for Semitransparent Perovskite Solar Cells with Engineered Bandgap Enables Efficiencies Exceeding 25% in Four-Terminal Tandems with Silicon and CIGS. *Adv. Funct. Mater.* **2020**, *30* (19), No. 1909919.

(11) Mei, A.; Sheng, Y.; Ming, Y.; Hu, Y.; Rong, Y.; Zhang, W.; Luo, S.; Na, G.; Tian, C.; Hou, X.; Xiong, Y.; Zhang, Z.; Liu, S.; Uchida, S.; Kim, T. W.; Yuan, Y.; Zhang, L.; Zhou, Y.; Han, H. Stabilizing Perovskite Solar Cells to IEC61215:2016 Standards with over 9,000-h Operational Tracking. *Joule* **2020**, *4* (12), 2646−2660.

(12) Zibouche, N.; Islam, M. S. Structure-Electronic Property Relationships of 2D Ruddlesden-Popper Tin- And Lead-Based Iodide Perovskites. *ACS Appl. Mater. Interfaces* **2020**, *12* (13), 15328−15337.

(13) Dou, J.; Bai, Y.; Chen, Q. Challenges of Lead Leakage in Perovskite Solar Cells. *Mater. Chem. Front.* **2022**, *6*, 2779−2789.

(14) Niu, G.; Guo, X.; Wang, L. Review of Recent Progress in Chemical Stability of Perovskite Solar Cells. *J. Mater. Chem. A* **2015**, *3* (17), 8970−8980.

(15) Rao, M. K.; Sangeetha, D. N.; Selvakumar, M.; Sudhakar, Y. N.; Mahesha, M. G. Review on Persistent Challenges of Perovskite Solar Cells' Stability. *Sol. Energy* **2021**, *218*, 469−491.

(16) Liu, Z.; Yang, H.; Wang, J.; Yuan, Y.; Hills-Kimball, K.; Cai, T.; Wang, P.; Tang, A.; Chen, O. Synthesis of Lead-Free Cs2AgBix6 (X = Cl, Br, I) Double Perovskite Nanoplatelets and Their Application in CO_2 Photocatalytic Reduction. *Nano Lett.* **2021**, *21* (4), 1620−1627.

(17) Wu, S. Q.; Cheng, S.; Lu, L.; Liu, M.; Jin, X. W.; Cheng, S. D.; Mi, S. B. B-Site Ordering and Strain-Induced Phase Transition in Double-Perovskite La2NiMnO6 Films. *Sci. Rep.* **2018**, *8* (1), 1−9.

(18) Matsuishi, K.; Suzuki, T.; Onari, S.; Gregoryanz, E.; Hemley, R. J.; Mao, H. K. Excitonic States of Alkylammonium Lead-Iodide Layered Perovskite Semiconductors under Hydrostatic Pressure to 25 GPa. *Phys. Status Solidi Basic Res.* **2001**, *223* (1), 177−182.

(19) Hsu, S. N.; Zhao, W.; Gao, Y.; Akriti; Segovia, M.; Xu, X.; Boudouris, B. W.; Dou, L. Thermoelectric Performance of Lead-Free Two-Dimensional Halide Perovskites Featuring Conjugated Ligands. *Nano Lett.* **2021**, *21* (18), 7839−7844.

(20) Hautzinger, M. P.; Raulerson, E. K.; Harvey, S. P.; Liu, T.; Duke, D.; Qin, X.; Scheidt, R. A.; Wieliczka, B. M.; Phillips, A. J.; Graham, K. R.; Blum, V.; Luther, J. M.; Beard, M. C.; Blackburn, J. L. Metal Halide Perovskite Heterostructures: Blocking Anion Diffusion with Single-Layer Graphene. *J. Am. Chem. Soc.* **2023**, *145* (4), 2052−2057.

(21) Ho, C. M.; Wu, M. C.; Chen, S. H.; Chang, Y. H.; Lin, T. H.; Jao, M. H.; Chan, S. H.; Su, W. F.; Lee, K. M. High-Performance Stable Perovskite Solar Cell via Defect Passivation With Constructing Tunable Graphitic Carbon Nitride. *Sol. RRL* **2021**, *5* (8), 1−13.

(22) Chueh, C. C.; Chen, C. I.; Su, Y. A.; Konnerth, H.; Gu, Y. J.; Kung, C. W.; Wu, K. C. W. Harnessing MOF Materials in

Photovoltaic Devices: Recent Advances, Challenges, and Perspectives. *J. Mater. Chem. A* **2019**, *7* (29), 17079−17095.
(23) Lee, C. C.; Chen, C. I.; Liao, Y. Te; Wu, K. C. W.; Chueh, C. C. Enhancing Efficiency and Stability of Photovoltaic Cells by Using Perovskite/Zr-MOF Heterojunction Including Bilayer and Hybrid Structures. *Adv. Sci.* **2019**, *6* (5), No. 1801715.
(24) Hoefler, S. F.; Trimmel, G.; Rath, T. Progress on Lead-Free Metal Halide Perovskites for Photovoltaic Applications: A Review. *Monatshefte fur Chemie* **2017**, *148* (5), 795−826.
(25) Wu, S.; Li, Z.; Li, M. Q.; Diao, Y.; Lin, F.; Liu, T.; Zhang, J.; Tieu, P.; Gao, W.; Qi, F.; Pan, X.; Xu, Z.; Zhu, Z.; Jen, A. K. Y. 2D Metal−Organic Framework for Stable Perovskite Solar Cells with Minimized Lead Leakage. *Nat. Nanotechnol.* **2020**, *15* (11), 934−940.
(26) Zhang, H.; Pfeifer, L.; Zakeeruddin, S. M.; Chu, J.; Grätzel, M. Tailoring Passivators for Highly Efficient and Stable Perovskite Solar Cells. *Nat. Rev. Chem.* **2023**, *7* (9), 632−652.
(27) Chang, T. H.; Kung, C. W.; Chen, H. W.; Huang, T. Y.; Kao, S. Y.; Lu, H. C.; Lee, M. H.; Boopathi, K. M.; Chu, C. W.; Ho, K. C. Planar Heterojunction Perovskite Solar Cells Incorporating Metal-Organic Framework Nanocrystals. *Adv. Mater.* **2015**, *27* (44), 7229−7235.
(28) Ji, J.; Liu, B.; Huang, H.; Wang, X.; Yan, L.; Qu, S.; Liu, X.; Jiang, H.; Duan, M.; Li, Y.; Li, M. Nondestructive Passivation of the TiO_2electron Transport Layer in Perovskite Solar Cells by the PEIE-2D MOF Interfacial Modified Layer. *J. Mater. Chem. C* **2021**, *9* (22), 7057−7064.
(29) Amrollahi Bioki, H.; Moshaii, A.; Borhani Zarandi, M. Performance Improvement of Ambient-Condition Fabricated Perovskite Solar Cells Using an Interfacial HKUST-1 MOF on Electron Transfer Layer. *Surfaces and Interfaces* **2021**, *27*, No. 101579.
(30) Chen, P.; Hou, J.; Wang, L. Metal-Organic Framework-Tailored Perovskite Solar Cells. *Microstructures* **2022**, *2* (3), 14.
(31) Cao, J.; Liu, C. K.; Piradi, V.; Loi, H. L.; Wang, T.; Cheng, H.; Zhu, X.; Yan, F. Ultrathin Self-Assembly Two-Dimensional Metal-Organic Framework Films as Hole Transport Layers in Ideal-Bandgap Perovskite Solar Cells. *ACS Energy Lett.* **2022**, *7* (10), 3362−3369.
(32) Kim, B. J.; Kim, M.; Lee, D. G.; Lee, G.; Bang, G. J.; Jeon, J. B.; Choi, M.; Jung, H. S. Interface Design of Hybrid Electron Extraction Layer for Relieving Hysteresis and Retarding Charge Recombination in Perovskite Solar Cells. *Adv. Mater. Interfaces* **2018**, *5* (23), No. 1800993.
(33) Xing, W.; Ye, P.; Lu, J.; Wu, X.; Chen, Y.; Zhu, T.; Peng, A.; Huang, H. Tellurophene-Based Metal-Organic Framework Nanosheets for High-Performance Organic Solar Cells. *J. Power Sources* **2018**, *401*, 13−19.
(34) Ma, J.; Wong-Foy, A. G.; Matzger, A. J. The Role of Modulators in Controlling Layer Spacings in a Tritopic Linker Based Zirconium 2D Microporous Coordination Polymer. *Inorg. Chem.* **2015**, *54* (10), 4591−4593.
(35) Bannwarth, C.; Caldeweyher, E.; Ehlert, S.; Hansen, A.; Pracht, P.; Seibert, J.; Spicher, S.; Grimme, S. Extended Tight-Binding Quantum Chemistry Methods. *Wiley Interdiscip. Rev. Comput. Mol. Sci.* **2021**, *11* (2), 1−49.
(36) Grimme, S.; Bannwarth, C.; Shushkov, P. A Robust and Accurate Tight-Binding Quantum Chemical Method for Structures, Vibrational Frequencies, and Noncovalent Interactions of Large Molecular Systems Parametrized for All Spd-Block Elements (Z = 1−86). *J. Chem. Theory Comput.* **2017**, *13* (5), 1989−2009.
(37) Enkovaara, J.; Rostgaard, C.; Mortensen, J. J.; Chen, J.; Dułak, M.; Ferrighi, L.; Gavnholt, J.; Glinsvad, C.; Haikola, V.; Hansen, H. A.; Kristoffersen, H. H.; Kuisma, M.; Larsen, A. H.; Lehtovaara, L.; Ljungberg, M.; Lopez-Acevedo, O.; Moses, P. G.; Ojanen, J.; Olsen, T.; Petzold, V.; Romero, N. A.; Stausholm-Møller, J.; Strange, M.; Tritsaris, G. A.; Vanin, M.; Walter, M.; Hammer, B.; Häkkinen, H.; Madsen, G. K. H.; Nieminen, R. M.; Nørskov, J. K.; Puska, M.; Rantala, T. T.; Schiøtz, J.; Thygesen, K. S.; Jacobsen, K. W. Electronic Structure Calculations with GPAW: A Real-Space Implementation of the Projector Augmented-Wave Method. *J. Phys.: Condens. Matter* **2010**, *22* (25), No. 253202.
(38) Shakiba, M.; Stippell, E.; Li, W.; Akimov, A. V. Nonadiabatic Molecular Dynamics with Extended Density Functional Tight-Binding: Application to Nanocrystals and Periodic Solids. *J. Chem. Theory Comput.* **2022**, *18* (9), 5157−5180.
(39) Akimov, A. V. Libra: An Open-source "Methodology Discovery" Library for Quantum and Classical Dynamics Simulations. *J. Comput. Chem.* **2016**, *37*, 1626−1649.
(40) Shakiba, M.; Smith, B.; Li, W.; Dutra, M.; Jain, A.; Sun, X.; Garashchuk, S.; Akimov, A. Libra: A Modular Software Library for Quantum Nonadiabatic Dynamics. *Softw. Impacts* **2022**, *14*, 100445.
(41) Kühne, T. D.; Iannuzzi, M.; Del Ben, M.; Rybkin, V. V.; Seewald, P.; Stein, F.; Laino, T.; Khaliullin, R. Z.; Schütt, O.; Schiffmann, F.; Golze, D.; Wilhelm, J.; Chulkov, S.; Bani-Hashemian, M. H.; Weber, V.; Borštnik, U.; Taillefumier, M.; Jakobovits, A. S.; Lazzaro, A.; Pabst, H.; Müller, T.; Schade, R.; Guidon, M.; Andermatt, S.; Holmberg, N.; Schenter, G. K.; Hehn, A.; Bussy, A.; Belleflamme, F.; Tabacchi, G.; Glöß, A.; Lass, M.; Bethune, I.; Mundy, C. J.; Plessl, C.; Watkins, M.; VandeVondele, J.; Krack, M.; Hutter, J. CP2K: An Electronic Structure and Molecular Dynamics Software Package - Quickstep: Efficient and Accurate Electronic Structure Calculations. *J. Chem. Phys.* **2020**, *152* (19), 194103.
(42) Stanton, R.; Gupta, S. K.; Trivedi, D. J. Probing Strain-Induced Effects on Performance of Low-Dimensional Hybrid Perovskites for Solar Energy Harvesting. *ACS Appl. Mater. Interfaces* **2022**, *14* (30), 34603−34611.
(43) Guo, L.; Xu, G.; Tang, G.; Fang, D.; Hong, J. Structural Stability and Optoelectronic Properties of Tetragonal MAPbI3 under Strain. *Nanotechnology* **2020**, *31* (22), 225204.
(44) Guo, W.; Yang, Z.; Dang, J.; Wang, M. Progress and Perspective in Dion-Jacobson Phase 2D Layered Perovskite Optoelectronic Applications. *Nano Energy* **2021**, *86* (April), No. 106129.
(45) Stanton, R.; Trivedi, D. J. Atomistic Description of the Impact of Spacer Selection on Two-Dimensional (2D) Perovskites: A Case Study of 2D Ruddlesden-Popper CsPbI3Analogues. *J. Phys. Chem. Lett.* **2022**, *13* (51), 12090−12098.
(46) Whitcher, T. J.; Zhu, J. X.; Chi, X.; Hu, H.; Zhao, D.; Asmara, T. C.; Yu, X.; Breese, M. B. H.; Castro Neto, A. H.; Lam, Y. M.; Wee, A. T. S.; Chia, E. E. M.; Rusydi, A. Importance of Electronic Correlations and Unusual Excitonic Effects in Formamidinium Lead Halide Perovskites. *Phys. Rev. X* **2018**, *8* (2), 1−10.
(47) Diroll, B. T. Temperature-Dependent Intraband Relaxation of Hybrid Perovskites. *J. Phys. Chem. Lett.* **2019**, *10* (18), 5623−5628.
(48) Chung, H.; Jung, S. Il; Kim, H. J.; Cha, W.; Sim, E.; Kim, D.; Koh, W.; Kim, J. Composition-dependent Hot Carrier Relaxation Dynamics in Cesium Lead Halide (CsPbX3, X= Br and I) Perovskite Nanocrystals. *Angew. Chem.* **2017**, *129* (15), 4224−4228.
(49) Yin, J.; Maity, P.; Naphade, R.; Cheng, B.; He, J. H.; Bakr, O. M.; Brédas, J. L.; Mohammed, O. F. Tuning Hot Carrier Cooling Dynamics by Dielectric Confinement in Two-Dimensional Hybrid Perovskite Crystals. *ACS Nano* **2019**, *13* (11), 12621−12629.
(50) Tully, J. C. Molecular Dynamics with Electronic Transitions. *J. Chem. Phys.* **1990**, *93* (2), 1061−1071.
(51) Smith, B.; Akimov, A. V. A Comparative Analysis of Surface Hopping Acceptance and Decoherence Algorithms within the Neglect of Back-Reaction Approximation. *J. Chem. Phys.* **2019**, *151* (12), 124107.
(52) Nelson, T.; Fernandez-Alberti, S.; Roitberg, A. E.; Tretiak, S. Nonadiabatic Excited-State Molecular Dynamics: Treatment of Electronic Decoherence. *J. Chem. Phys.* **2013**, *138* (22), 224111.
(53) Akimov, A. V.; Prezhdo, O. V. Advanced Capabilities of the PYXAID Program: Integration Schemes, Decoherence Effects, Multiexcitonic States, and Field-Matter Interaction. *J. Chem. Theory Comput.* **2014**, *10* (2), 789−804.
(54) Trivedi, D. J.; Prezhdo, O. V. Decoherence Allows Model Reduction in Nonadiabatic Dynamics Simulations. *J. Phys. Chem. A* **2015**, *119* (33), 8846−8853.
(55) Martínez, L.; Andrade, R.; Birgin, E. G.; Martínez, J. M. PACKMOL: A Package for Building Initial Configurations for

https://doi.org/10.1021/acs.nanolett.3c04054
Nano Lett. XXXX, XXX, XXX−XXX

Molecular Dynamics Simulations. *J. Comput. Chem.* **2009**, *30* (13), 2157−2164.
(56) Stanton, R.; Trivedi, D. J. Pyrovskite: A Software Package for the High-Throughput Construction, Analysis, and Featurization of Two- and Three-Dimensional Perovskite Systems. *J. Chem. Phys.* **2023**, *159* (6), 64803.

https://doi.org/10.1021/acs.nanolett.3c04054
Nano Lett. XXXX, XXX, XXX−XXX